
Short-term orbital effects of radiation pressure on the Lunar Reconnaissance Orbiter

Dominik Stiller

B.Sc. Student, Faculty of Aerospace Engineering, TU Delft, Netherlands

Abstract

Centimeter-scale orbit determination is necessary for satellite navigation and spaceborne geodesy. Orbits are sensitive to perturbations such as radiation pressure (RP) due to solar radiation as well as planetary albedo and thermal emissions. This project investigated sensitivities of orbit predictions to varying complexity in RP models for the Lunar Reconnaissance Orbiter (LRO). We found that solar RP dominates but lunar RP affects secular variations in semi-major axis and argument of periapsis. A constant-albedo lunar model and a paneled LRO model are recommended for precise radial and along-track positioning.

Acronyms: BRDF bidirectional reflectance distribution function; DLAM-1 Delft Lunar Albedo Model 1; LRO Lunar Reconnaissance Orbiter; RP radiation pressure

1 Introduction

Describe LRO mission
Describe need for POD
sub-meter accuracy in radial component [1] 50-100 m in total position [2]

figure with magnitudes of perturbations

”SRP is the largest non-gravitational perturbation affecting the LRO orbit and inadequate modeling of SRP is the primary cause of large prediction errors for LRO, particularly during high-beta angle periods” [3] albedo modeling on moon necessary for selenodetic mapping [4] albedo radiation significant on moon since no atmosphere exists and surface of lunar highlands is rather reflective % [4] High OD error during full-sun periods with cannonball model, but acceptable with multi-panel model and real attitude for SA and HGA [5]

present similar papers like VielbergKusche

in this paper, only investigate orbital variations over 2.5 day arc - ζ goal is to improve force models for POD Long-term effect of RP would also be interesting (forces could cancel out over time or always act in same direction), but not considered here

Tudat is used and models are used for future research

2 Radiation pressure modeling

RP modeling needs to consider the causes and effects of radiation. This section presents a range of cooperating models for both that can be flexibly composed.

2.1 Mechanics of radiation pressure

RP results from the momentum transfer between electromagnetic radiation and a surface. A spacecraft may receive such radiation from the Sun but also from other celestial bodies: planets and moons emit albedo radiation through reflection of sunlight and thermal radiation depending on surface temperature. The RP exerts a force on the spacecraft

governed by surface properties such as area, reflectivity and absorptivity. The resulting acceleration is the result of a complex interplay of the bodies emitting radiation (the “sources”) and the spacecraft receiving the radiation (the “target”).

Radiation can characterized by the radiant flux density, which commonly has units of W/m^2 . Radiosity is the *emitted and reflected* radiant flux density of an opaque surface. The irradiance E is the *incident* radiant flux density on a surface and provides a convenient way to decouple source and target models: the irradiance and the direction of incidence are sufficient to determine the target acceleration, independent of the actual source. We can combine this information into a vector quantity which we call directional irradiance $\mathbf{E} = E\hat{\mathbf{r}}_{t/s}$, where $\hat{\mathbf{r}}_{t/s}$ is the unit vector in the source-to-target direction. One or more directional irradiances, which can be thought of as light rays, are the output of a source model and used as input to the target model. The RP exerted on an irradiated surface is proportional to $1/c$, where $c = 299\,792\,458 \text{ m/s}$ is the speed of light. Given the magnitude of c , RP is usually small (around $4.5 \times 10^{-6} \text{ N/m}^2$ for solar radiation at Earth, where $E = 1361 \text{ W/m}^2$ [6]).

Electromagnetic radiation is often composed not just of a single wavelength but rather a range of wavelengths. The distribution can be described by the spectral irradiance in units of $\text{W}/(\text{m}^2 \text{Hz})$. Since surface properties are often wavelength-dependent, the target model would also have to be aware of the distribution. However, the surface properties as a function of wavelength are often not known, which is also the case for LRO. Therefore, we assume the irradiance from source models to be integrated over the whole spectrum and the surface properties of the target model to be valid for all wavelengths.

2.2 Reflectance distribution

Describing the reflectance of a surface is key to RP modeling. Both the way a source reflects sunlight and the direction a

⁰Email: dstiller@uw.edu

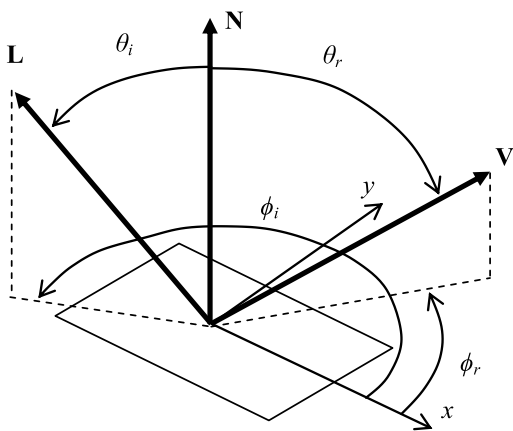


Figure 1. Geometry of a BRDF for a surface with normal \mathbf{N} , incoming direction \mathbf{L} , and observer direction \mathbf{V} . The viewing angle θ_r is between \mathbf{N} and \mathbf{V} . The phase angle (not labeled) is between \mathbf{L} and \mathbf{V} . Adapted from [7].

target is accelerated in depend on the angular distribution of reflectance.

General reflectance distribution In general, reflectance comprises a diffuse (scattered in many directions) and a specular (mirror-like) component. The remaining energy is absorbed by the surface. The reflectance varies with surface normal \mathbf{N} , incoming radiation direction \mathbf{L} , and observer direction \mathbf{V} . This geometry is shown in Figure 1. A bidirectional reflectance distribution function (BRDF) describes the fraction of irradiance reflected towards the observer per steradian, i.e. [7]

$$f_r(\theta_i, \phi_i, \theta_r, \phi_r) = \frac{dL_r(\theta_r, \phi_r)}{dE_j(\theta_i, \phi_i)}, \quad (1)$$

where dL_r is the reflected radiance (the directional counterpart to radiosity, typically in $\text{W}/(\text{m}^2 \text{sr})$) and dE_j is the received irradiance.

The planetary surface BRDF directly leads to the albedo irradiance received by a target if the sun irradiance at the planet surface and the solid angle subtended by the target are known.

The target surface BRDF gives the direction in which the target is accelerated through integration over all directions \mathbf{V} in which radiation is reflected. The unitless reaction vector, which includes both the direction and magnitude based on absorbed, specularly and diffusely reflected fractions, is therefore [7]

$$\mathbf{R} = - \left[\mathbf{L} + \int_0^{2\pi} \int_0^{\pi/2} f_r \cos \theta_r \mathbf{V} d\theta_r d\phi_r \right]. \quad (2)$$

This vector encapsulates the mechanics of momentum transfer. The reaction is minimal for pure absorption ($f_r = 0$). The reaction is maximal (double the minimum) for pure specular reflection in the incidence direction.

Specular-diffuse reflectance distribution A simplified BRDF is usually more practical for RP modeling: the reflectance is assumed to be a mix of an ideal Lambertian diffuse component and a purely mirror-like specular

components. Such a BRDF is given by [7]

$$f_r = C_d \frac{1}{\pi} + C_s \frac{\delta(\mathbf{V} - \mathbf{M})}{\cos \theta_i} \quad (3)$$

where C_d and C_s are the diffuse and specular reflectivity coefficients. Together with the absorption coefficient C_a , energy is conserved when $C_a + C_d + C_s = 1$. The vector $\mathbf{M} = 2 \cos \theta_i \mathbf{N} - \mathbf{L}$ is the direction of \mathbf{L} 's mirror-like reflection, which only contributes if $\mathbf{V} = \mathbf{M}$.

For this simplified BRDF, the integral in Equation (2) evaluates analytically to [8]

$$\mathbf{R} = - \left[(C_a + C_d) \mathbf{L} + \frac{2}{3} C_d \mathbf{N} + 2 \cos \theta_i C_s \mathbf{N} \right]. \quad (4)$$

If the target is in thermodynamic equilibrium, all absorbed radiation will be reradiated instantaneously by Kirchhoff's law. If this reradiation is Lambertian, the reaction vector becomes [8]

$$\mathbf{R} = - \left[(C_a + C_d) \left(\mathbf{L} + \frac{2}{3} \mathbf{N} \right) + 2 \cos \theta_i C_s \mathbf{N} \right]. \quad (5)$$

The specular contribution is strictly along the surface normal direction since its tangential components cancel. The Lambertian diffuse contribution (both reflected and reradiated) has a component along the incoming direction but also, weighted by a factor 2/3 (see [9] for a derivation of this factor), a component along the surface normal. The reaction vector will thus always be in the plane spanned by \mathbf{L} and \mathbf{N} .

2.3 Radiation sources

Radiation sources emit or reflect radiation, which exerts RP onto the target. As explained in Section 2.1, the incident radiation at a target due to a source can be thought of as light rays, which are described by their directional irradiance at the target. How the directional irradiance is calculated depends on the type of source.

Isotropic point sources The simplest source model is a point source that isotropically radiates in all directions. This model is appropriate for far-away sources such as the Sun at 1 au distance. Due to the distance, all rays are effectively parallel and can be merged into a single ray parallel to the source-to-target vector $\mathbf{r}_{t/s}$. For an isotropic source, the total luminosity L (units of W) is uniformly distributed over a sphere, leading to an inverse square law. Therefore, the irradiance at the target is

$$E = \frac{L}{4\pi \|\mathbf{r}_{t/s}\|^2}. \quad (6)$$

Alternatively, a reference irradiance E_{ref} observed at a distance \mathbf{r}_{ref} can be scaled:

$$E = E_{\text{ref}} \frac{r_{\text{ref}}}{\|\mathbf{r}_{t/s}\|^2}. \quad (7)$$

The solar luminosity is $3.828 \times 10^{26} \text{ W}$ [10], which corresponds to an irradiance of 1361 W/m^2 at 1 au. Note that these values are averages, which vary with the 11-year solar cycle by about 0.1% and more on shorter timescales due to sunspot darkening and facular brightening [11]. Observational time series exist to account for these variations [12].

Paneled sources: *Discretization* Radiation due to planets and moons requires more involved source models. Planetary emissions comprise reflected solar radiation and thermal infrared radiation [13]. The fraction of reflected sunlight is called albedo¹ a ; the corresponding type is therefore also called albedo radiation. Thermal radiation is due to absorbed solar energy that is re-emitted in a delayed fashion. Observation time series of albedo and thermal fluxes exist for Earth [12], but physical modeling is required for the Moon.

Since planetary radiation is not isotropic and the spacecraft is typically much closer to the body than to the Sun, the source extent has to be considered. In contrast to the previously described point source, we therefore model Earth and Moon as extended sources. These are discretized into sub-sources, from which rays emanate that are, in general, not parallel. The sub-sources can be thought of as panels with an area, orientation, position, and radiosity model. The panel extent is represented by the area but any other panel properties are only evaluated at its center. A panel only radiates from the positive normal side, not from the backside.

Different algorithms exist to divide the planet ellipsoid into panels. Some authors use a longitude–latitude grid (e.g., [15, 16]), particularly with observed fluxes) or generate static, uniformly spaced panels over the whole sphere (e.g., [7]). However, both approaches are inefficient for low-altitude spacecraft, which require a large number of panels, most of which are never visible. Therefore, the de-facto standard is the dynamic² paneling method introduced by Knocke *et al.* [13].

In Knocke’s method, only the visible area of the planet is paneled. This area is a spherical cap, centered at the subsatellite point and divided into concentric rings that are, again, divided into equal-area segments. A central panel is located at the subsatellite point. All panels contribute to the irradiance received by the target. However, the effective area of each panel is projected by its viewing angle θ_r (see Figure 1) and the irradiance is attenuated by an inverse square law. In Knocke’s method, the rings are spaced such that each panel has the same projected, attenuated area. The projected, attenuated area of a panel is defined as [13]

$$\frac{dA \cos \theta_r}{\|\mathbf{r}_{t/s}\|^2}, \quad (8)$$

where dA is the geometric panel area and $r_{t/s}$ is the source-to-target vector (in this case, the panel-to-target vector). More rings and more panels per ring will improve the fidelity of the calculated irradiance, barring the resolution limit of the radiosity model (e.g., the albedo distribution). While arbitrary numbers of panels per ring are possible, Knocke suggests multiples of 6 (i.e., six panels in the first ring, twelve panels in the second ring, . . .). The algorithm is elaborated in [17].

Two examples at different spacecraft altitudes and with different ring numbers are shown in Figure 2. At higher altitudes, a larger area is visible (approaching a hemisphere) and panels are somewhat more uniform in area. At lower altitudes, the panels are more tightly spaced towards the subsatellite point. In both cases, panel areas increase towards the edge of the visible cap. This pattern is result of the equal projected, attenuated areas.

Paneled sources: *Radiosity models* The emitted and reflected fluxes of a panel are described by a radiosity model. The irradiance at the target position can then be derived from the panel radiosity. Both radiosity and irradiance commonly have units of W/m^2 . Each panel can have one or more radiosity model, usually one for albedo radiation and one for thermal radiation. We will now present three such models.

The albedo radiosity model accounts for diffuse Lambertian reflection of solar radiation. It implements the specular-diffuse BRDF from Equation (3) with $C_s = 0$ and the albedo value $C_d = a$ at the panel center. The albedo radiosity of a panel is [13]

$$J_{\text{albedo}} = a (\cos \theta_i)_+ E_s, \quad (9)$$

where E_s is the incoming solar irradiance at the panel (e.g., as found from Equation (6)) and the solar incidence angle θ_i is defined in Figure 1. The operator $(\cdot)_+$ restricts the input to positive values or zero otherwise. This ensures that no radiation is reflected from the backside.

The delayed thermal radiosity model assumes that absorbed radiation is emitted independently of incident solar radiation and the radiosity is thus not a function of θ_i . The only spatial variations arise from emissivity differences. The emissivity e of a surface is the ratio of the actual radiosity to the ideal black body radiosity. The delay arises from the planet’s large thermal inertia. The delayed thermal radiosity of a panel is [13]

$$J_{\text{thermal}} = e \frac{E_s}{4}, \quad (10)$$

where e is the emissivity of the panel, evaluated at its center. The factor 1/4 is the ratio of absorbing area (a circle) to emitting area (a sphere). The albedo and delayed thermal model were originally used by Knocke *et al.* for Earth emissions [13].

The angle-based thermal radiosity model is more appropriate than the delayed model if the surface experience significant diurnal cooling and heating. The surface temperature is modeled as a function of the solar incidence angle θ_i and related to the radiosity through the Stefan-Boltzmann law. The surface temperature is interpolated between the minimum and maximum temperatures, T_{\min} and T_{\max} as

$$T = \max \left(T_{\max} (\cos \theta_i)_+^{1/4}, T_{\min} \right). \quad (11)$$

These temperatures typically correspond to the nighttime temperature and the temperature at the subsolar point. The angle-based thermal radiosity of a panel is then [18]

$$J_{\text{thermal}} = e \sigma T^4, \quad (12)$$

¹Two types of albedo exist: spherical/Bond albedo is the fraction of sunlight reflected in all directions, while geometrical albedo is the fraction of sunlight reflected with respect to an ideal diffuse surface for normal incidence and viewing directions [14]. For our purpose, spherical albedo is appropriate and will be used synonymously with albedo in this paper.

²Dynamic refers to the fact that panels move with the spacecraft, as opposed to static paneling, for which panels are invariant with spacecraft position or time.

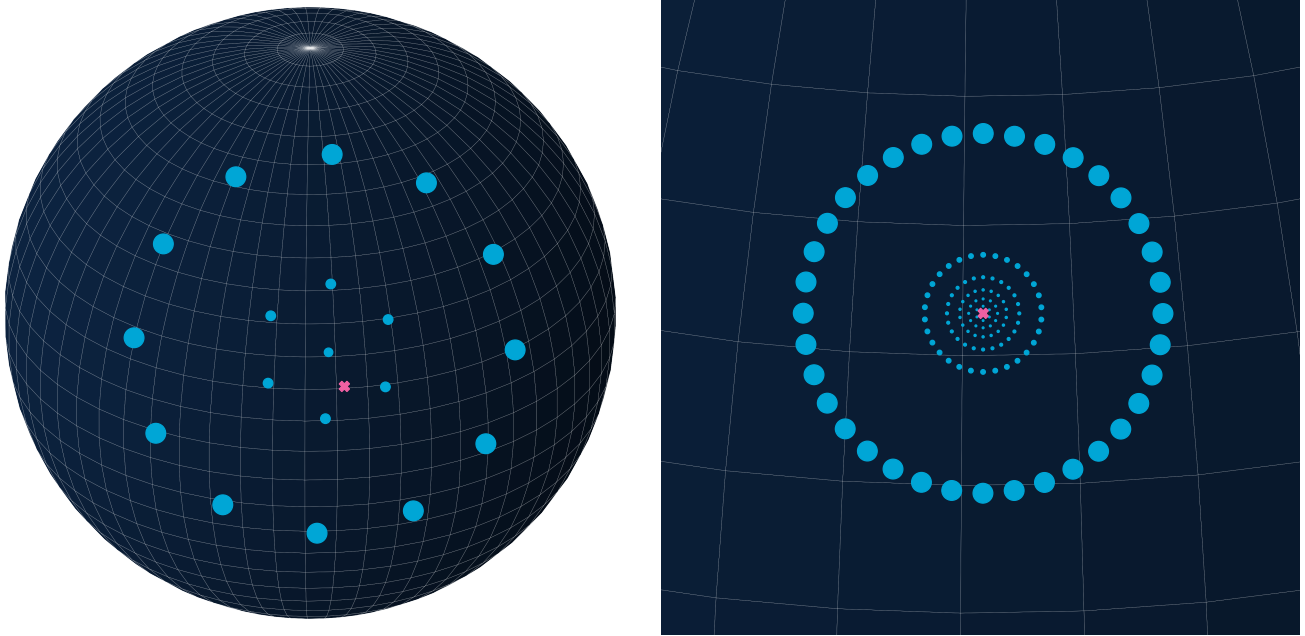


Figure 2. Panels generated with Knocke’s algorithm for the Moon, which has a polar radius of 1737 km. The spacecraft (\star) sees a spherical cap (—), which contains rings of panels and is larger at higher altitudes h . Panel centers (●) are scaled proportional to the panel area. The panels have equal projected, attenuated areas and are therefore concentrated around the subsatellite point. The scenario in **b** corresponds to LRO’s orbit and the paneling used in this paper.

where T is the surface temperature from Equation (11) at the panel center and $\sigma = 5.670 \times 10^{-8} \text{ W}/(\text{m}^2 \text{ K}^4)$ is the Stefan–Boltzmann constant. On the dayside, the radiosity is proportional to $T_{\max}^4 \cos \theta_i$. The maximum radiosity of $e\sigma T_{\max}^4$ is usually larger than the near-constant $eE_s/4$ from Equation (10), but quickly decreases as the panel moves away from the subsolar point (where $\theta_i = 0^\circ$). On the nightside, the thermal radiosity reduces to $e\sigma T_{\min}^4$.

The albedo and thermal radiosity models depend on the distribution of a and e over the planetary surface. The values may be assumed constant but generally vary with longitude, latitude, and time. Particularly for Earth, seasons and weather greatly affect reflectivity and emissivity [19]. Since the Moon lacks seasons, distributions that only vary spatially are appropriate.

To obtain the irradiance at the target due to the panel radiosity, we assume that the emission follows Lambert’s cosine law and account for the projected, attenuated area of the source panel. The irradiance therefore is

$$E = \left(\sum_{J_i \in \mathcal{J}} J_i \right) \frac{dA (\cos \theta_r)_+}{\pi \| \mathbf{r}_{t/s} \|^2}, \quad (13)$$

where \mathcal{J} is the set of radiosities from any of the previous radiosity models. Usually, a panel has the albedo model and one thermal model. Here, the source-to-target vector $\mathbf{r}_{t/s}$ uses the panel center position, not the source body center. The direction $\hat{\mathbf{r}}_{t/s}$ of the corresponding directional irradiance $\mathbf{E} = E \hat{\mathbf{r}}_{t/s}$ is therefore not the same for each panel and thus considers the extent of the source. The radiosities J_i in Equation (13) can be summed since their radiation emanates from the same point, the panel center. Contrarily, the directional irradiances \mathbf{E} can generally not be summed since the their individual directions need to be

retained: the reflectance model of the target may be sensitive to the incoming direction of each ray. Therefore, a set of directional irradiances \mathcal{E} is handed to the RP target model for acceleration calculations.

2.4 Radiation pressure targets

A RP target is a body that is accelerated by RP. The target model governs how the incident irradiances from point sources and extended sources accelerate the target body.

Cannonball target In its simplest form, a target can be modeled as isotropic sphere, also referred to as cannonball. This sphere is characterized by a cross-sectional area A_c (independent of orientation), radiation pressure coefficient C_r (incorporating reflectivity and absorption coefficients), and mass m . Due to its isotropy, any lateral components cancel and the net acceleration is always along the source-to-target vector. The RP acceleration of a cannonball target is [20]

$$\mathbf{a} = C_r \frac{A_c}{m} \sum_{\mathbf{E}_j \in \mathcal{E}} \frac{\mathbf{E}_j}{c}, \quad (14)$$

where the sum is vectorial and $\sum \mathbf{E}_j/c$ is the total RP as described in Section 2.1. \mathcal{E} is the set of directional irradiances from any number of sources, both point (Equation (6)) and paneled (Equation (13)). The dependence on the area-to-mass ratio A_c/m is similar to drag accelerations. While the cannonball model cannot account for complex geometry, it is often used in orbit determination with C_r as estimated variable. Ray tracing of a detailed model can also be used to establish the evolution of A_c and C_r [21].

Paneled target In reality, the cross-section and optical properties of a spacecraft change with orientation and

incident direction. This effect is particularly noticeable for solar panels, which are large and usually track the Sun. To account for the geometry and differences in materials, a spacecraft can be represented as a collection of n panels. Each panel is characterized by its area, surface normal, and reflectance distribution. The position would only be relevant for rotational but not for linear accelerations. In case of moving parts, the surface normal may change over time. The reflectance distribution can be given as generic BRDF, but is often a specular-diffuse BRDF. The RP acceleration of a paneled target is [22]

$$\mathbf{a} = \frac{1}{m} \sum_{\mathbf{E}_j \in \mathcal{E}} \left(\frac{\|\mathbf{E}_j\|}{c} \sum_{k=1}^n A_k (\cos \theta_{i,k})_+ \mathbf{R}_k \right), \quad (15)$$

where the indices j and k denote the (sub-)source and target panel, respectively. A_k is the area of the k -th panel. $\theta_{i,k}$ is the incidence angle of \mathbf{E}_i onto the k -th panel. \mathbf{R}_k is the reaction vector as defined by Equations (2), (4) or (5), depending on the BRDF. The reaction vector is a function of the panel surface normal \mathbf{N} and the source-to-target direction $\mathbf{L} = \hat{\mathbf{E}}_j$. Therefore, the inner sum has to be evaluated for each directional irradiance \mathbf{E}_j of the outer sum. In general, the resulting acceleration will not be along the source-to-target direction as for the cannonball.

Extensions for the paneled target model exist. The model described above does not account for self-shadowing, which occurs when one ray would intersect two panels. This effectively reduces the area of the shadowed panel, an effect that can be significant for complex spacecraft geometries [23]. Polygon intersections enable simple calculation of the effective area [23]. Ray tracing is more involved but can also account for multiple reflections between target panels [24].

Another extension is the radiation pressure due to thermal radiation of the spacecraft itself. Instantaneous reradiation as modeled by Equation (5) for the case of thermodynamic equilibrium is a simple version of this. In reality, panels heat up and cool down (particularly during eclipses) through radiation, conduction, and internal heat production. Advanced models therefore calculate the temperature of each panel. Such models range from a simple heat balance [7] to finite element models [16]. However, lack of knowledge of the thermal properties may restrict the applicability. For the sake of simplicity, neither self-shadowing nor thermal radiation pressure of the spacecraft will be considered in this paper.

2.5 Occultation

All previous models assume that the line of sight between source and target is unobstructed. However, occultation is a common astronomical phenomenon: a low-altitude spacecraft may be in the planet's shadow for more than a third of its orbit, and partial or full lunar eclipses can occur multiple times per year. We present two occultation models.

Shadow function The shadow function ν describes the fraction of light received from a spherical source in the presence of an occulting spherical body. The geometry of the conical occultation model is shown in Figure 3. In the umbra, the source is fully occulted and the observer does not receive any radiation ($\nu = 0$), a state referred to as total

eclipse. In the penumbra, the observer can see part of the source ($0 < \nu < 1$). Only outside the shadow region does the observer receive the full radiation ($\nu = 1$). In the case of a lunar eclipse, Earth occults the Sun and casts a shadow onto the Moon such that there is no lunar albedo radiation. On the nightside of a planet, the planet itself occults the Sun.

With the models described in Sections 2.3 and 2.4, the shadow function needs to be considered for radiation from a point source, both when directly incident on the target and when used as solar radiation for albedo radiosity. The extent of the source and occulting bodies needs to be known for shadow function calculations, even in the case of point sources. A derivation of the conical model for ν is presented by Montenbruck and Gill [20].

The conical model can only account for one occulting body. In case of multiple occulting bodies, shadows might overlap and the product of their shadow functions would underestimate the actual received fraction. Knowledge of the shadow intersection would be required to avoid this. Zhang *et al.* derived a model for two occulting bodies [26]. However, only single occultations will be considered in this paper.

More involved shadow models exist that improve prediction of the penumbra passage. These models can consider planetary oblateness and atmospheric effects like absorption, scattering and refraction [27]. Other models can account for topography by combining a paneled Sun model with a topography map [28]. These modifications usually prolong the penumbra duration.

Point-to-point visibility For source panels represented by their center point, the shadow function becomes binary: either there is a line of sight between the panel center and the target or there is not. Such point-to-point visibility with a spherical occulting body is easily modeled geometrically. A derivation is given by Vallado and Wertz [25]. Multiple occultations are supported in this occultation model by the logical conjunction of the individual visibilities.

3 Radiation pressure modeling for LRO

TODO write intro

3.1 Lunar albedo radiation

The Moon is a major source of radiation in LRO's orbit, with lunar irradiance magnitudes approaching half of the Sun's. Therefore, albedo and thermal radiation due to the Moon will be modeled. While the lunar albedo is only 40 % of

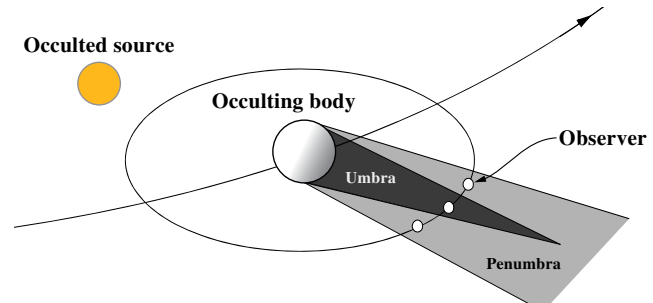
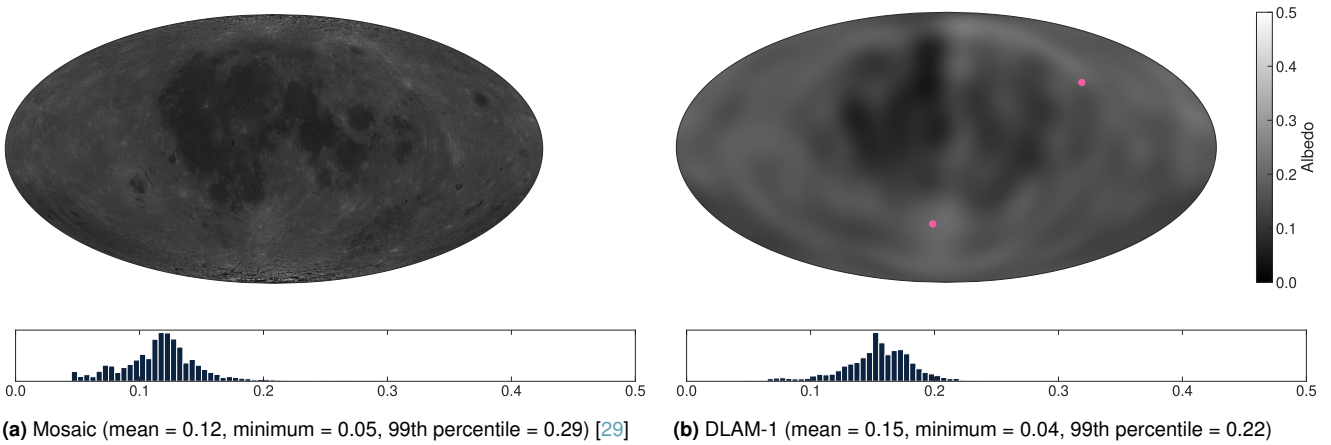


Figure 3. Conical occultation model for spherical sources and occulting bodies. The observer is partially illuminated in the penumbra but fully shadowed in the umbra. Adapted from [25].



(a) Mosaic (mean = 0.12, minimum = 0.05, 99th percentile = 0.29) [29]

(b) DLAM-1 (mean = 0.15, minimum = 0.04, 99th percentile = 0.22)

Figure 4. Lunar albedo distribution from Clementine. Both the mosaic and DLAM-1 are based on 750 nm reflectivity, but DLAM-1 has been corrected to the average solar wavelength. Large bright features like the Tycho and Giordano Bruno craters (●) can be registered. Note that the maximum of the albedo scale here is 0.5 instead of 1.0 to increase contrast; in reality, the Moon appears half as bright.

Earth's albedo [19], albedo radiation due to the Moon is still substantial, particularly over the subsolar point [4]. Lunar albedo varies significantly with geology: the highlands (mean $a = 0.16$, maximum $a = 0.25$) are much more reflective than the maria (mean $a = 0.07$, minimum $a = 0.05$) due to their respective regolith composition [30–32]. The mosaic of calibrated albedo imagery from Clementine in Figure 4a clearly shows the differences between highlands and maria. The mean of 0.12 agrees with other literature [30], and most of the lunar surface has an albedo below 0.20. Higher values are only found at the poles, where the imagery represents topographic shading rather than actual albedo [33]. Note that the mosaic is for albedo of light at 750 nm wavelength, which is slightly longer than the average solar wavelength. Even though solar radiation has most energy within the 300 nm to 2400 nm band, the spectrum peaks at around 470 nm [34]. Lunar reflectivity increases with increasing wavelength [35].

Floberghagen *et al.*'s 15×15 spherical harmonics expansion called Delft Lunar Albedo Model 1 (DLAM-1) [4] is often used to represent this spatial albedo variability in lunar RP models. DLAM-1 was fitted from Clementine imagery and was designed to work with Knocke's albedo model for dynamic paneling (Equation (9)). Due to the nature of spherical harmonics, the model cannot resolve features smaller than 12° (360 km at the equator). The expansion is shown in Figure 4b, along with direct imagery from Clementine. DLAM-1 was also derived from 750 nm imagery, but we scale the original values by 1/1.3 to account for the reduced reflectivity at the average solar wavelength. This factor was proposed by Vasavada *et al.* [30]. Even with the correction, the mean albedo of the expansion of 0.15 is still 25 % above the commonly accepted mean of 0.12. This is possibly due to a different calibration of the imagery that DLAM-1 is based on compared to the mosaic from Figure 4a. In fact, Clementine is known to overestimate albedo due to bad calibration [35]. Apart from the difference in magnitude, the patterns agree reasonably well: maria and highlands are distinct and large bright features like the ray system around the Tycho and Giordano Bruno craters can be recognized (marked in Figure 4b).

Despite the shortcomings of DLAM-1, spherical harmonics are convenient: they are smooth and do not require interpolation like a gridded map. They can easily be truncated to trade detail for computational efficiency. Therefore, we will use DLAM-1 in this paper but consider that the magnitude may be overestimated by 25 % during the analysis of results. We will also compare results for the location-dependent DLAM-1 with those for a constant value, which should be more computationally efficient. As single representative albedo, we choose the mean of 0.15 instead of 0.12 to facilitate comparison. Note that the spatial variability described above suggests that a single albedo value cannot accurately represent lunar reflectivity.

Albedo radiation assumes ideal, diffuse Lambertian reflectance, which decreases with the cosine of the viewing angle. This assumption is especially appropriate for Earth, for which purely specular radiosity only amounts to 10 % of the purely diffuse radiosity [13]. However, this is not the case for the Moon: the opposition effect increases the reflectance at low phase angles (when the source is behind the observer, see Figure 3) much more than would be expected from a cosine law. In fact, the brightness increases more than 40 % between phase angles of 4° and 0° [36]. This is primarily caused by shadow hiding. To account for non-diffuse reflectance of the lunar surface, the Hapke BRDF was developed [37]. This BRDF is an empirical relation based on nine parameters that control, among other phenomena, the strength and directionality of the opposition effect. Near-global maps for these parameters have been fitted from LRO observations and could be used for a radiosity model [32]. For RP acceleration modeling, the opposition effect is only of concern when the target is above the subsolar point; the Sun has to be in the orbital plane for this. For LRO, this only occurs for a few days twice a year, and even then only for a small fraction of the orbit. Therefore, we will neglect opposition effect in this study.

3.2 Lunar thermal radiation

Lunar surface temperatures and the associated thermal radiation undergoes a significant diurnal cycle. Daytime and nighttime temperatures can differ by up to 290 K. The surface

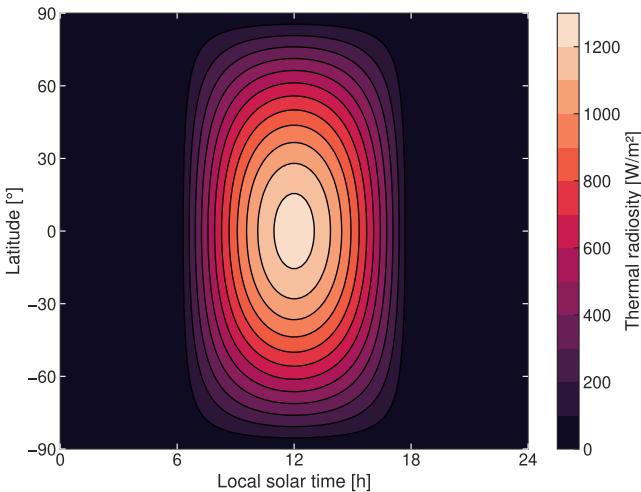


Figure 5. Map of lunar thermal emissions from the angle-based model (Equation (12)). The emissivity is 0.95 and surface temperatures range between 95 K and 385 K, depending on the subsolar angle.

heats rapidly after sunrise, cools at about the same rate after local noon, then slower during the night [30]. There are small seasonal changes, with the noon temperature differing by 6 K between lunar aphelion and perihelion [14]. The large diurnal variability makes Knocke’s delayed thermal model (Equation (10)), which gives a constant radiosity throughout the day, unsuitable for the Moon.

Diurnal variability is represented well by the angle-based thermal model (Equation (12)). We parametrize the model with the equatorial temperatures just before sunrise ($T_{\min} = 95$ K) and at local noon ($T_{\max} = 385$ K). The model transitions to the nighttime temperature when the incidence angle $\theta_i \geq 89.8^\circ$. The temperatures span a slightly larger range than Lemoine *et al.* ($T_{\min} = 100$ K, $T_{\max} = 375$ K), who initially proposed the angle-based model. However, they agree with those used by Park *et al.* [38]. Note that Park *et al.*’s model is identical up to a factor 1/4 in the radiosity, which is incorrect.

While the albedo varies with location (see Section 3.1), the emissivity and other thermophysical properties are remarkably uniform [31]. This means that a constant emissivity is a fair assumption. We use a value of $e = 0.95$, which is the broadband daytime emissivity, although it decreases to 0.90 during the night [39]. However, we assume the constant daytime emissivity at all times.

The thermal surface radiosity J_{thermal} from the angle-based model with the aforementioned parameters is shown in Figure 5. The radiosity decreases with the cosine of the incidence angle and approaches negligible emissions of 6 W/m² at nighttime. The maximum radiosity, which occurs below the subsolar point (i.e., at local noon), is 1246 W/m². This peak value agrees with those used to design LRO’s thermal control subsystem [40]. The only effect that is not captured is the slow cooling by about 25 K between sunset and sunrise [30], which introduces a slight asymmetry; we use constant pre-sunrise temperatures throughout the night. We also do not model seasonal variations of surface temperature.

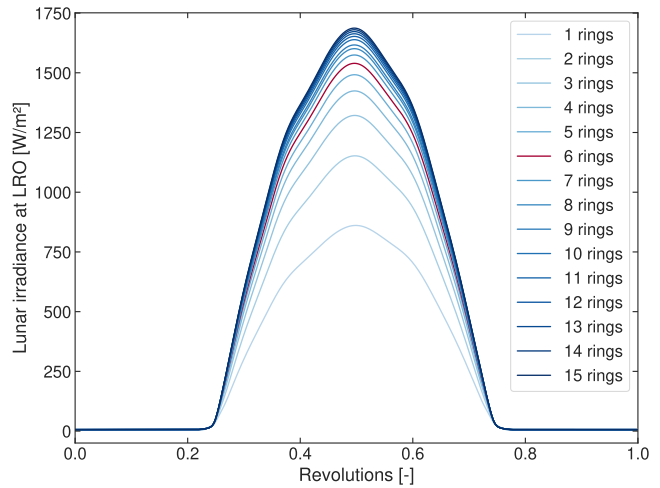


Figure 6. Convergence of lunar irradiance received by LRO for increasing number of rings. Each ring contains six more panels than the previous one. Six rings (—) are sufficient for an error of less than 10 % with respect to the converged solution.

3.3 Paneling of the Moon

Knocke’s dynamic paneling method described in Section 2.3 will be used for the Moon. LRO’s low altitude compared to the lunar radios prohibits any static paneling, which would have a large number of never-visible panels.

Selecting the number of rings is a trade-off between fidelity and computational efficiency. To determine the lowest number of rings that can still represent lunar radiation with sufficient accuracy, we investigated the convergence behavior. Figure 6 shows the albedo and thermal irradiance received by LRO for an increasing number of rings. As suggested by Knocke *et al.*, each ring contains six more panels than the previous one. For 13 rings and more, the peak irradiance is within 1 % of 1687 W/m². For six rings, the irradiance peaks at 1540 W/m², which is within 10 % of the converged solution. The results are similar for constant and DLAM-1 albedo.

We choose six rings as sufficiently accurate, which contain 127 panels in total. The panel geometry in this case was already shown in Figure 2b. This is one ring (or 36 panels) more than used by others. Floberghagen *et al.* suggests five rings for Lunar Prospector, which has twice the orbital altitude of LRO and thus needs fewer rings (Knocke *et al.* only used two rings for a much higher altitude relative to the planetary radios). Five rings are also used for LRO’s operational orbit determination [41]. We choose one ring more to keep the error due to paneling below 10 %. A higher number may be required in case of a higher-resolution albedo distribution.

3.4 LRO target

LRO consists of a cubical bus with a large solar array and a protruding high gain antenna (Figure 7). The solar array tracks the Sun in two axes, and the antenna points towards Earth whenever it is visible. This leads to large variations in cross-section over time, and different sides are presented to incoming solar and lunar radiation.

LRO can be modeled as paneled target (Equation (15)) to account for this variability. The panels are summarized in

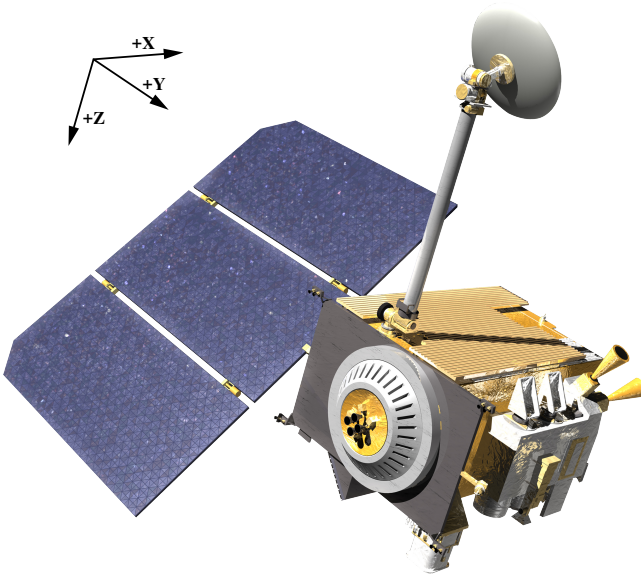


Figure 7. Rendering of LRO [42] including bus frame definition. The X axis is along the velocity vector, the +Y axis is the anti-sun side, and the +Z axis is in the nadir direction [40].

Table 1. There are six panels for the bus, with surface normals along the positive and negative axes of the LRO bus frame (cf. Figure 7). The solar array and high gain antenna are modeled separately, again with frontside and backside panels. The solar array is almost as large as all other panels combined. Since it always points towards Sun, the solar RP will have a large effect. Note that, while tracking of the solar array and antenna are constrained to two axes in reality, we allow three-axis tracking for simplicity. The definitive attitudes of both are also available but were not used since their data volume is prohibitively large. We also neglect self-shadowing, which was shown to only have a minor impact in most cases [3, 44], but can be significant for solar radiation [23].

We also model LRO as a cannonball (Equation (14)), a model which is often used for orbit determination. Finding a single equivalent cross-section area A_c and RP coefficient C_r is virtually impossible [25]. Different values for LRO exist in literature: Bauer *et al.* use $A_c = 10 \text{ m}^2$ and $C_r = 1.2$ [45], while Nicholson *et al.* use $A_c = 14 \text{ m}^2$ and $C_r = 1.0$ [41]. Their acceleration should differ by about 15 %. We choose

Table 1. Panels for LRO target model from Smith *et al.* [43]. The coefficients are for absorptivity and specular/diffuse reflectivity. The solar array is by far the largest surface, followed by the Z-facing panels.

| Panel | C_a | C_s | C_d | $A [\text{m}^2]$ |
|-------|-------|-------|-------|------------------|
| +X | 0.49 | 0.29 | 0.22 | 2.82 |
| -X | 0.42 | 0.39 | 0.19 | 2.82 |
| +Y | 0.45 | 0.32 | 0.23 | 3.69 |
| -Y | 0.50 | 0.32 | 0.18 | 3.69 |
| +Z | 0.50 | 0.32 | 0.18 | 5.14 |
| -Z | 0.28 | 0.54 | 0.18 | 5.14 |
| +SA | 0.90 | 0.05 | 0.05 | 11.00 |
| -SA | 0.50 | 0.30 | 0.20 | 11.00 |
| +HGA | 0.54 | 0.18 | 0.28 | 1.00 |
| -HGA | 0.93 | 0.02 | 0.05 | 1.00 |

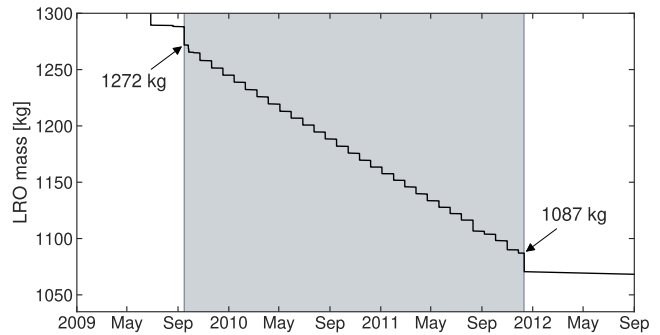


Figure 8. Mass evolution of LRO over the science mission phase (15 September 2009 – 11 December 2011, ■).

the latter since it is used for operational orbit estimation of LRO.

To complete the target model, the mass is required to convert forces into accelerations. LRO performed monthly station keeping maneuvers during its science mission phase, which reduced the initial mass after science orbit insertion from 1272 kg to 1087 kg (Figure 8). With every maneuver, 6.3 kg of propellant are expelled [46]. This increases accelerations by 15 % over the course of 21 months. To facilitate comparison and obtain worst-case results, we will use the end-of-mission mass of 1087 kg in this paper, independently of the actual arc.

3.5 LRO orbit geometry

LRO's polar science mission orbit has a low altitude of $50 \pm 15 \text{ km}$. The difference between periselene and apiselene is mostly due to a slight eccentricity, but also due to an equatorial radios that is 2 km larger than the polar radius. The altitude variation affects the lunar irradiance received by LRO. The spacecraft has a period of 113 min.

Visibility of the Sun is determined by the beta angle β , which is the angle between the orbital plane and the Moon-to-Sun vector. It is zero when the Sun is within the plane and $\pm 90^\circ$ when the orbit normal points towards the Sun. Since LRO's orbit is polar, it undergoes all β within a year. For $\beta = 0^\circ$, LRO is moving towards and away from the Sun above the polar, experiences the maximum eclipse duration, and passes over the subsolar point. For $\beta = 90^\circ$, LRO is in full view of the Sun throughout the orbit, and there is no along-track component of the solar radiation. The spacecraft does not pass over hot or well-illuminated lunar regions.

Since the effect of RP varies greatly with β , we will investigate two arcs in this paper. They are summarized in Table 2. In June, Moon is at aphelion and no eclipses occur. In September, the beta angle is just below 0° ; LRO will experience the maximum solar eclipse duration of 48 min. No lunar eclipses occur during any of the arcs. Both arcs have

Table 2. Orbit geometry for selected arcs over 2.5 days. The June arc gives full illumination, the September arc the maximum eclipse duration.

| | 28 June 2010 | 26 Sept. 2011 |
|--------------------|--------------|----------------|
| $\beta [^\circ]$ | 88.8 to 88.9 | -1.71 to -3.56 |
| Sun distance [au] | 1.019 | 1.000 |
| Eclipse time [min] | 0 | 48 |

a length of 2.5 days, which is used for orbit determination of LRO [41, 47]. Choosing the same length ensures our results are relevant for error estimation in force modeling for orbit determination.

3.6 Simulation setup

simulation setup in table, explanations in text

earth albedo + thermal radiation can be neglected for LRO since it is less than 0.1% of solar radiation at moon

solar array tracks Sun, HGA tracks Earth [40] start at start at 26 June 2010 06:00:00 Earth eclipses Sun during this time Moon does not eclipse Sun (Sun beta angle is about -90 deg, see [40])

occultations lunar eclipses avoided since we cannot represent multiple occultations

effects of neglecting terrain and self shadowing [28] sec 4.2 and 4.3

Operational LRO OD does not use lunar albedo due to computational demand, but used for offline reprocessing. Self-shadowing from Mazarico *et al.* is used for reprocessing [41]

step 5 s, which is also used for LRO orbit determination [28]

MOON_PA frame, IAU_MOON is in worst case 155 m off [48] (Special PCK and FK for Earth and Moon, slide 14)

integrator + propagator params

two arcs, one for beta = 0 and beta = 90 describe why These

4 Results

no knowledge of true RP accelerations therefore, compare to baseline

Also use [49] as reference for plots and discussion, especially about relation of acc and change in elements

4.1 Simulation setups

Solar with/without Lunar with/without Albedo constant/dlam LRO cannonball/paneled Occultation with/without (for solar only?) with/without instantaneous reradiation

4.2 Instantaneous reradiation

show difference in magnitude and difference in shape conclude that difference in shape is for most part negligible but difference in magnitude not since no reradiation is unrealistic, use it going forward Thermal radiation may cause an offset of 1-2 meters over an arclength of 2.5 days [45]

4.3 Accelerations

thermal vs albedo

define along track, cross, radial

kink in cross-track SRP also seen in SELENE [50], search for explanation

Variation with orbital position and time of year (correlate with relative sun position and albedo map)

beta angle slightly less than 90 degrees leads to sinusoidal acceleration

show partial/full eclipse on time axis

absolute acceleration magnitude influenced by mass uncertainty rp acceleration magnitude increases as mass

decreases 17% higher mass at start - ζ 17 % lower acceleration magnitude

angle-based thermal behaves quite similar to albedo, but does not vanish in eclipse

cross track sign depends on sign of beta - ζ direction not super meaningful, also for orbital elements (e.g. change in lon asc node)

albedo likely overestimated by 25% as described in Section 3.1

4.4 Change in final position

Thermal in the range of a few meters [47]

4.5 Change in orbital element

compare wih Gauss perturbing equations (analytical solution to change of osculating elements based on accelerations), e.g. [51, Sec. 3.2]

4.6 Performance

no special setup like cpu pinning or disabled hyperthreading for benchmarking only on one setup Performance may vary in other situations [52] still, a good indication also mention minimum

albedo model can increase computational demand by several hundred pct [41]

5 Discussion & Conclusion

"It would seem, therefore, that the influence of the longwave emitted radiation would be almost indistinguishable from a small change in the gravitational constant of the Earth, for low eccentricity orbits. As a consequence, one would expect the shortwave component to have a greater orbital effect than the longwave component, in spite of the comparable magnitudes of their accelerations." [17]

magnitude affected by:

- wrong mass
- overestimated albedo
- number of rings
- for cannonball, choice of A and C

recommendations on which models to use

Future work:

- account for moon topography for occlusion [28], could otherwise lead to large misrepresentation of eclipses for $\beta > 70^\circ$
- Self-shadowing, particularly for SRP, can reduce effective cross section by up to 40% [28]
- fit new SH albedo model or just use map
- accurate thermal reradiation (e.g. [53])
- account for non-diffuse reflection of lunar surface, i.e. opposition effect due to shadow hiding and coherent backscatter, which can greatly increase irradiance at small phase angles [36] (this would only be relevant at beta = 0 since low phase angles do not occur for large betas; phase angle is low if target is above subsolar point); a map of Hapke parameters exists [32]

References

1. M. T. Zuber *et al.*, “The Lunar Reconnaissance Orbiter Laser Ranging Investigation,” *Space Science Reviews*, vol. 150, no. 1-4, pp. 63–80, May 2009. DOI: [10.1007/s11214-009-9511-z](https://doi.org/10.1007/s11214-009-9511-z).
2. G. Chin *et al.*, “Lunar Reconnaissance Orbiter Overview: The Instrument Suite and Mission,” *Space Science Reviews*, vol. 129, no. 4, pp. 391–419, May 2007. DOI: [10.1007/s11214-007-9153-y](https://doi.org/10.1007/s11214-007-9153-y).
3. S. Slojkowski, J. Lowe, and J. Woodburn, “Orbit determination for the lunar reconnaissance orbiter using an extended Kalman filter,” in *International Symposium on Space Flight Dynamics (ISSFD) 2015*, 2015.
4. R. Floberghagen, P. Visser, and F. Weischede, “Lunar albedo force modeling and its effect on low lunar orbit and gravity field determination,” *Advances in Space Research*, vol. 23, no. 4, pp. 733–738, Jan. 1999. DOI: [10.1016/s0273-1177\(99\)00155-6](https://doi.org/10.1016/s0273-1177(99)00155-6).
5. S. E. Slojkowski, “Lunar Reconnaissance Orbiter orbit determination accuracy analysis,” in *International Symposium on Space Flight Dynamics*, 2014.
6. G. Kopp and J. L. Lean, “A new, lower value of total solar irradiance: Evidence and climate significance,” *Geophysical Research Letters*, vol. 38, no. 1, n/a–n/a, Jan. 2011. DOI: [10.1029/2010gl045777](https://doi.org/10.1029/2010gl045777).
7. C. J. Wetterer *et al.*, “Refining Space Object Radiation Pressure Modeling with Bidirectional Reflectance Distribution Functions,” *Journal of Guidance, Control, and Dynamics*, vol. 37, no. 1, pp. 185–196, Jan. 2014. DOI: [10.2514/1.60577](https://doi.org/10.2514/1.60577).
8. O. Montenbruck, P. Steigenberger, and U. Hugentobler, “Enhanced solar radiation pressure modeling for Galileo satellites,” *Journal of Geodesy*, vol. 89, no. 3, pp. 283–297, Nov. 2014. DOI: [10.1007/s00190-014-0774-0](https://doi.org/10.1007/s00190-014-0774-0).
9. M. Ziebart, “Generalized Analytical Solar Radiation Pressure Modeling Algorithm for Spacecraft of Complex Shape,” *Journal of Spacecraft and Rockets*, vol. 41, no. 5, pp. 840–848, Sep. 2004. DOI: [10.2514/1.13097](https://doi.org/10.2514/1.13097).
10. A. Prša *et al.*, “NOMINAL VALUES FOR SELECTED SOLAR AND PLANETARY QUANTITIES: IAU 2015 RESOLUTION B3,” *The Astronomical Journal*, vol. 152, no. 2, p. 41, Aug. 2016. DOI: [10.3847/0004-6256/152/2/41](https://doi.org/10.3847/0004-6256/152/2/41).
11. G. Kopp, “Magnitudes and timescales of total solar irradiance variability,” *Journal of Space Weather and Space Climate*, vol. 6, A30, 2016. DOI: [10.1051/swsc/2016025](https://doi.org/10.1051/swsc/2016025).
12. S. Dewitte and N. Clerbaux, “Measurement of the Earth Radiation Budget at the Top of the Atmosphere—A Review,” *Remote Sensing*, vol. 9, no. 11, p. 1143, Nov. 2017. DOI: [10.3390/rs9111143](https://doi.org/10.3390/rs9111143).
13. P. Knocke, J. Ries, and B. Tapley, “Earth radiation pressure effects on satellites,” in *Astrodynamic Conference*, American Institute of Aeronautics and Astronautics, Aug. 1988. DOI: [10.2514/6.1988-4292](https://doi.org/10.2514/6.1988-4292).
14. G. Heiken and B. M. French, *Lunar Sourcebook, A User’s Guide to the Moon*. Cambridge University Press, 1991.
15. C. J. Rodriguez-Solano, U. Hugentobler, P. Steigenberger, and S. Lutz, “Impact of Earth radiation pressure on GPS position estimates,” *Journal of Geodesy*, vol. 86, no. 5, pp. 309–317, Oct. 2011. DOI: [10.1007/s00190-011-0517-4](https://doi.org/10.1007/s00190-011-0517-4).
16. F. Wöske, T. Kato, B. Rievers, and M. List, “GRACE accelerometer calibration by high precision non-gravitational force modeling,” *Advances in Space Research*, vol. 63, no. 3, pp. 1318–1335, Feb. 2019. DOI: [10.1016/j.asr.2018.10.025](https://doi.org/10.1016/j.asr.2018.10.025).
17. P. Knocke, “Earth radiation pressure effects on satellites,” Ph.D. dissertation, The University of Texas at Austin, 1989.
18. F. G. Lemoine *et al.*, “High-degree gravity models from GRAIL primary mission data,” *Journal of Geophysical Research: Planets*, vol. 118, no. 8, pp. 1676–1698, Aug. 2013. DOI: [10.1002/jgre.20118](https://doi.org/10.1002/jgre.20118).
19. P. R. Goode *et al.*, “Earthshine observations of the Earth’s reflectance,” *Geophysical Research Letters*, vol. 28, no. 9, pp. 1671–1674, May 2001. DOI: [10.1029/2000gl012580](https://doi.org/10.1029/2000gl012580).
20. O. Montenbruck and E. Gill, *Satellite Orbits*. Springer Berlin Heidelberg, Dec. 2000, 371 pp. DOI: [10.1007/978-3-642-58351-3](https://doi.org/10.1007/978-3-642-58351-3).
21. A. Hattori and T. Otsubo, “Time-varying solar radiation pressure on Ajisai in comparison with LAGEOS satellites,” *Advances in Space Research*, vol. 63, no. 1, pp. 63–72, Jan. 2019. DOI: [10.1016/j.asr.2018.08.010](https://doi.org/10.1016/j.asr.2018.08.010).
22. J. Marshall, S. Luthcke, P. Antreasian, and G. Rosborough, “Modeling radiation forces acting on TOPEX/Poseidon for precision orbit determination,” Goddard Space Flight Center, Tech. Rep. NASA-TM-104564, 1992.
23. E. Mazarico, M. T. Zuber, F. G. Lemoine, and D. E. Smith, “Effects of Self-Shadowing on Nonconservative Force Modeling for Mars-Orbiting Spacecraft,” *Journal of Spacecraft and Rockets*, vol. 46, no. 3, pp. 662–669, May 2009. DOI: [10.2514/1.41679](https://doi.org/10.2514/1.41679).
24. P. W. Kenneally and H. Schaub, “Fast spacecraft solar radiation pressure modeling by ray tracing on graphics processing unit,” *Advances in Space Research*, vol. 65, no. 8, pp. 1951–1964, Apr. 2020. DOI: [10.1016/j.asr.2019.12.028](https://doi.org/10.1016/j.asr.2019.12.028).
25. D. A. Vallado and J. Wertz, *Fundamentals of Astrodynamics and Applications*, 4th ed. Microcosm Press, 2013, p. 1106.
26. R. Zhang, R. Tu, P. Zhang, J. Liu, and X. Lu, “Study of satellite shadow function model considering the overlapping parts of Earth shadow and Moon shadow and its application to GPS satellite orbit determination,” *Advances in Space Research*, vol. 63, no. 9, pp. 2912–2929, May 2019. DOI: [10.1016/j.asr.2018.02.002](https://doi.org/10.1016/j.asr.2018.02.002).
27. Z. Li, M. Ziebart, S. Bhattacharai, and D. Harrison, “A shadow function model based on perspective projection and atmospheric effect for satellites in eclipse,” *Advances in Space Research*, vol. 63, no. 3, pp. 1347–1359, Feb. 2019. DOI: [10.1016/j.asr.2018.10.027](https://doi.org/10.1016/j.asr.2018.10.027).

28. E. Mazarico, G. A. Neumann, M. K. Barker, S. Goossens, D. E. Smith, and M. T. Zuber, "Orbit determination of the Lunar Reconnaissance Orbiter: Status after seven years," *Planetary and Space Science*, vol. 162, pp. 2–19, Nov. 2018. DOI: [10.1016/j.pss.2017.10.004](https://doi.org/10.1016/j.pss.2017.10.004).
29. USGS Astrogeology Science Center. "Moon Clementine UVVIS Global Mosaic 118m v2." (Apr. 9, 2009), [Online]. Available: https://astrogeology.usgs.gov/search/map/Moon/Clementine/UVVIS/Lunar_Clementine_UVVIS_750nm_Global_Mosaic_118m_v2.
30. A. R. Vasavada *et al.*, "Lunar equatorial surface temperatures and regolith properties from the Diviner Lunar Radiometer Experiment," *Journal of Geophysical Research: Planets*, vol. 117, no. E12, n/a–n/a, Apr. 2012. DOI: [10.1029/2011je003987](https://doi.org/10.1029/2011je003987).
31. P. O. Hayne *et al.*, "Global Regolith Thermophysical Properties of the Moon From the Diviner Lunar Radiometer Experiment," *Journal of Geophysical Research: Planets*, vol. 122, no. 12, pp. 2371–2400, Dec. 2017. DOI: [10.1002/2017je005387](https://doi.org/10.1002/2017je005387).
32. H. Sato, M. S. Robinson, B. Hapke, B. W. Denevi, and A. K. Boyd, "Resolved Hapke parameter maps of the Moon," *Journal of Geophysical Research: Planets*, vol. 119, no. 8, pp. 1775–1805, Aug. 2014. DOI: [10.1002/2013je004580](https://doi.org/10.1002/2013je004580).
33. A. McEwen and M. Robinson, "Mapping of the Moon by Clementine," *Advances in Space Research*, vol. 19, no. 10, pp. 1523–1533, Jan. 1997. DOI: [10.1016/s0273-1177\(97\)00365-7](https://doi.org/10.1016/s0273-1177(97)00365-7).
34. M. Iqbal, *Introduction to Solar Radiation*. Academic Press Canada, 1983.
35. Y. Shkuratov, V. Kaydash, V. Korokhin, Y. Velikodsky, N. Opanasenko, and G. Videen, "Optical measurements of the Moon as a tool to study its surface," *Planetary and Space Science*, vol. 59, no. 13, pp. 1326–1371, Oct. 2011. DOI: [10.1016/j.pss.2011.06.011](https://doi.org/10.1016/j.pss.2011.06.011).
36. B. J. Buratti, J. K. Hillier, and M. Wang, "The Lunar Opposition Surge: Observations by Clementine," *Icarus*, vol. 124, no. 2, pp. 490–499, Dec. 1996. DOI: [10.1006/icar.1996.0225](https://doi.org/10.1006/icar.1996.0225).
37. B. Hapke, *Theory of reflectance and emittance spectroscopy*. Cambridge University Press, 2012.
38. R. S. Park *et al.*, "Estimating a High-Resolution Lunar Gravity Field and Time-Varying Core Signature," in *AGU Fall Meeting Abstracts*, vol. 2011, Dec. 2011, P44B-06, P44B-06.
39. J. L. Bandfield, P. O. Hayne, J.-P. Williams, B. T. Greenhagen, and D. A. Paige, "Lunar surface roughness derived from LRO Diviner Radiometer observations," *Icarus*, vol. 248, pp. 357–372, Mar. 2015. DOI: [10.1016/j.icarus.2014.11.009](https://doi.org/10.1016/j.icarus.2014.11.009).
40. C. R. Tooley *et al.*, "Lunar Reconnaissance Orbiter Mission and Spacecraft Design," *Space Science Reviews*, vol. 150, no. 1-4, pp. 23–62, Jan. 2010. DOI: [10.1007/s11214-009-9624-4](https://doi.org/10.1007/s11214-009-9624-4).
41. A. Nicholson, S. Slojkowski, A. Long, M. Beckman, and R. Lamb, "NASA GSFC Lunar Reconnaissance Orbiter (LRO) Orbit Estimation and Prediction," in *SpaceOps 2010 Conference*, American Institute of Aeronautics and Astronautics, Apr. 2010. DOI: [10.2514/6.2010-2328](https://doi.org/10.2514/6.2010-2328).
42. NASA Science Mission Directorate. "Spacecraft Icons." (2018), [Online]. Available: <https://science.nasa.gov/get-involved/toolkits/spacecraft-icons>.
43. D. Smith, M. Zuber, F. Lemoine, M. Torrence, and E. Mazarico, "Orbit determination of LRO at the Moon," in *7th Int. Laser Ranging Service Workshop*, 2008, pp. 13–17.
44. A. Löcher and J. Kusche, "Precise orbits of the Lunar Reconnaissance Orbiter from radiometric tracking data," *Journal of Geodesy*, vol. 92, no. 9, pp. 989–1001, Feb. 2018. DOI: [10.1007/s00190-018-1124-4](https://doi.org/10.1007/s00190-018-1124-4).
45. S. Bauer *et al.*, "Demonstration of orbit determination for the Lunar Reconnaissance Orbiter using one-way laser ranging data," *Planetary and Space Science*, vol. 129, pp. 32–46, Sep. 2016. DOI: [10.1016/j.pss.2016.06.005](https://doi.org/10.1016/j.pss.2016.06.005).
46. M. Mesarch, M. Beckman, D. Folta, R. Lamb, and K. Richon, "Maneuver Operations Results from the Lunar Reconnaissance Orbiter (LRO) Mission," in *SpaceOps 2010 Conference*, American Institute of Aeronautics and Astronautics, Apr. 2010. DOI: [10.2514/6.2010-1985](https://doi.org/10.2514/6.2010-1985).
47. E. Mazarico *et al.*, "Orbit determination of the Lunar Reconnaissance Orbiter," 3, vol. 86, Springer Science and Business Media LLC, Sep. 2011, pp. 193–207. DOI: [10.1007/s00190-011-0509-4](https://doi.org/10.1007/s00190-011-0509-4).
48. Navigation and Ancillary Information Facility, *SPICE Tutorials*, Jan. 2020.
49. N. Borderies and P.-y. Longaretti, "A new treatment of the albedo radiation pressure in the case of a uniform albedo and of a spherical satellite," *CELESTIAL MECHANICS AND DYNAMICAL ASTRONOMY*, vol. 49, no. 1, pp. 69–98, 1990. DOI: [10.1007/bf00048582](https://doi.org/10.1007/bf00048582).
50. T. Kubo-oka and A. Sengoku, "Solar radiation pressure model for the relay satellite of SELENE," *Earth, Planets and Space*, vol. 51, no. 9, pp. 979–986, Sep. 1999. DOI: [10.1186/bf03351568](https://doi.org/10.1186/bf03351568).
51. D. M. Lucchesi and V. Iafolla, "The Non-Gravitational Perturbations impact on the BepiColombo Radio Science Experiment and the key rôle of the ISA accelerometer: direct solar radiation and albedo effects," *Celestial Mechanics and Dynamical Astronomy*, vol. 96, no. 2, pp. 99–127, Oct. 2006. DOI: [10.1007/s10569-006-9034-9](https://doi.org/10.1007/s10569-006-9034-9).
52. T. Mytkowicz, A. Diwan, M. Hauswirth, and P. F. Sweeney, "Producing wrong data without doing anything obviously wrong!" *ACM SIGPLAN Notices*, vol. 44, no. 3, pp. 265–276, Feb. 2009. DOI: [10.1145/1508284.1508275](https://doi.org/10.1145/1508284.1508275).
53. J. A. Marshall and S. B. Luthcke, "Modeling radiation forces acting on Topex/Poseidon for precision orbit determination," *Journal of Spacecraft and Rockets*, vol. 31, no. 1, pp. 99–105, Jan. 1994. DOI: [10.2514/3.26408](https://doi.org/10.2514/3.26408).